9A.4 A HYBRID ENSEMBLE KALMAN FILTER APPROACH TO DATA ASSIMILATION IN A TWO-DIMENSIONAL SHALLOW WATER MODEL

Lili Lei* and David R. Stauffer

Pennsylvania State University, University Park, PA

1. INTRODUCTION

Evensen (1994) first proposed the ensemble Kalman filter (EnKF) in an oceanographic application, and the ensemble Kalman filter techniques have since been implemented in atmospheric applications by Houtekamer and Mitchell (1998), Anderson (2001) and Whitaker and Hamill (2002). The background error covariances in the EnKF are computed from an ensemble forecast. Thus the EnKF is able to provide a flow-dependent estimate of the background error covariances for use in data assimilation.

The EnKF, an intermittent data assimilation scheme, performs a data-assimilation analysis at each observation time and switches back to standard model integration between analysis times. This cycle of a model integration period, analysis step, and then another model integration period often causes discontinuities / error spikes between the observation times (e.g., Hunt et al. 2004). The discontinuities may be related to dynamic imbalances caused every time a new observation is incorporated into the background model analysis. In the study of Fujita et al. (2007), the discontinuities of errors before and after the analysis step are shown to occur when hourly surface observations are assimilated by EnKF. A logical question may be whether their reported RMS wind errors increasing through the 6-h assimilation period reflect in some way enhanced divergence related to gravity-wave activity caused by the hourly updates. There are also discontinuities reported in the forward and backward Kalman filter analyses as discussed in Juckes and Lawrence (2009). Duane et al. (2006) also found the Kalman filter algorithm has some desynchronization bursts at times of regime transitions between the Lorenz and "reversed Lorenz" phases.

Based on the results in these studies, we hypothesize that if the EnKF is able to be applied continuously in time, analyses can be improved by reducing the discontinuities or bursts. Nudging, or Newtonian relaxation, is a continuous data assimilation scheme designed to be applied every time step, allowing corrections to be made gradually within a time window around the observation times (Stauffer and Seaman 1990; 1994). Thus a hybrid EnKF scheme that combines both EnKF and nudging was proposed and tested in the Lorenz three-variable model by Lei and Stauffer (2007; 2008). The hybrid EnKF uses nudging-type terms to apply the EnKF gradually in time in order to minimize the insertion shocks. In this study, the hybrid EnKF is extended from the Lorenz three-variable model to use a more realistic two-dimensional (2D) shallow water model for two types of cases: a quasi-stationary wave and a moving vortex.

* *Corresponding author address:* Lili Lei, Department of Meteorology, 503 Walker Building, Pennsylvania State University, University Park, PA 16802-5013; e-mail: lzl130@psu.edu.

2. THE HYBRID EnKF SCHEME

To apply the EnKF continuously in time rather than at only the analysis time, the hybrid EnKF combines the EnKF (Evensen 1994; Houtekamer and Mitchell 1998) and the observation nudging method (Stauffer and Seaman 1990; 1994). Figure 1 illustrates the hybrid EnKF technique. Suppose we start with an ensemble of N background forecasts that will be updated by the EnKF and a forecast that will be updated by the nudging (called the "nudging state"). The following five steps are repeated for each data assimilation cycle: 1) Compute the hybrid nudging coefficients using the ensemble forecast via the EnKF algorithm. 2) Compute the nudging state by continuously applying nudging with the hybrid nudging coefficients. 3) Update each of the ensemble members using the EnKF. 4) Shift the ensemble from its ensemble mean to the analysis of the nudging state while retaining the ensemble spread. 5) Integrate the ensemble and the nudging state forward to the next analysis time.

The nudging scheme adds additional relaxation terms into the governing model equations. The full set of model equations is then used to nudge the model state towards the observation state gradually, as shown by Eq. (1):

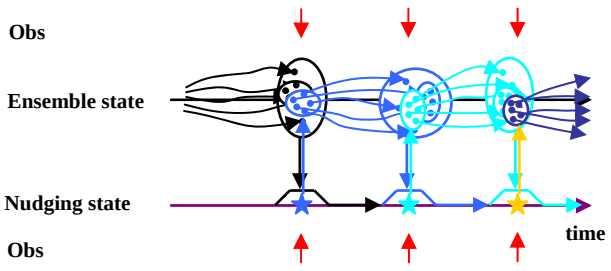

Figure 1. A schematic illustrating the five steps per assimilation cycle of the hybrid EnKF described in the text. The small dots denote the ensemble members, the ellipses around the small dots denote the ensemble spread, and the curved arrows indicate the trajectory of the ensemble members. The stars denote the analyses of the nudging state at the observation times, and the trapezoids show the nudging time window. The observations are denoted by the red arrows.

$$\frac{d\,\vec{\mathrm{x}}}{dt} = f\left(\vec{\mathrm{x}}\right) + \mathrm{G}\cdot \mathrm{w}_s \cdot \mathrm{w}_t \cdot \left(\vec{\mathrm{x}}^o - \vec{\mathrm{x}}\right), \qquad (1)$$

where $\vec{\mathrm{x}}$ and f are the state vector and standard forcing function of the system, $\vec{\mathrm{x}}^o$ is the observation, G is the nudging magnitude matrix, and w_s and w_t are the spatial and temporal weighting coefficients. The product of G, w_s and w_t is defined here as the nudging coefficient.

The nudging magnitude matrix is usually set to nonzero diagonal elements and zero off-diagonal elements. The nonzero diagonal elements are often specified by past experience and experimentation (Stauffer and Seaman 1994). The flow-dependent hybrid nudging coefficients, computed from the ensemble forecast (Lei and Stauffer 2007; 2008), are elements of the EnKF gain matrix normalized by the sum of the temporal weighting coefficient over the assimilation window. The flow-dependent hybrid nudging coefficient is described by Eq. (2):

$$\mathrm{G}\cdot \mathrm{w}_s = \frac{1}{\sum_t \mathrm{w}_t \cdot \Delta t} \cdot \mathrm{K}\,, \qquad (2)$$

where Δt is the time step and K is the EnKF gain matrix.

Thus the hybrid EnKF scheme takes advantage of ensemble forecasts and its flow-dependent / time-dependent background error covariances to provide flow-dependent / time-varying nudging coefficients. The hybrid EnKF also extends the nudging magnitude matrix from having nonzero diagonal elements and zero off-diagonal elements to a full nonzero matrix. This form may lead to a smoother, more accurate adjustment of the model background to the observations than does the nudging scheme or EnKF applied separately.

3. EXPERIMENTAL DESIGN

3.1 *Model and initial conditions*

As an extension of our previous work with the Lorenz three-variable system (Lei and Stauffer 2007; 2008), experiments in this study are performed using a more realistic 2D shallow water model. The barotropic nonlinear shallow water equations take the following form:

$$\begin{aligned}
&\frac{\partial u}{\partial t} + u\frac{\partial u}{\partial x} + v\frac{\partial u}{\partial y} - fv = -g\frac{\partial h}{\partial x} + \kappa\nabla^2 u \\
&\frac{\partial v}{\partial t} + u\frac{\partial v}{\partial x} + v\frac{\partial v}{\partial y} + fu = -g\frac{\partial h}{\partial y} + \kappa\nabla^2 v \\
&\frac{\partial h}{\partial t} + u\frac{\partial h}{\partial x} + v\frac{\partial h}{\partial y} = -h\left(\frac{\partial u}{\partial x} + \frac{\partial v}{\partial y}\right) + \kappa\nabla^2 h \\
&0 \le x \le L\,, \quad 0 \le y \le D\,,
\end{aligned} \qquad (3)$$

where u and v are the velocity components in the x and y directions, h is the depth of the fluid, g is the acceleration of gravity, f is the Coriolis parameter, κ is the diffusion coefficient, and L and D are the dimensions of the rectangular domain of integration. The Coriolis parameter f is defined as constant 10^{-4} s^{-1} using the f -plane approximation. The diffusion coefficient κ is given as 10^4 m^2s^{-1}.

The domain dimensions L and D are set to 500 km and 300 km, respectively. The grid spacing in the x and y directions is 10 km. Thus the grid dimensions are 52×31. The time step is 30 s and a leapfrog scheme is used to integrate the model in time.

The hybrid EnKF is tested in two cases: a quasi-stationary wave (Case I) and a moving vortex (Case II). Reduced acceleration of gravity g is used in the quasi-stationary wave case, and defined as 0.5 ms^{-2}. The true initial condition of Case I follows Grammeltvedt (1969) and Zhu et al. (1994). The true initial height is given by:

$$\begin{aligned}
h(x,y) = H_0 + H_1 * \tanh\left(\frac{9*(D/2-y)}{2D}\right) \\
+ H_2 * \mathrm{sech}^2\left(\frac{9*(D/2-y)}{D}\right) * \sin\left(\frac{2\pi}{L}\right)
\end{aligned}\,, \qquad (4)$$

where H_0, H_1 and H_2 are set to 50.0 m, 5.5 m, and 3.325 m respectively. The true initial wind field is derived from the initial height field assuming geostrophy. The true initial height and wind fields are shown by Fig. 2a.

A phase error (2π/8) is added into Eq. (4) to create the initial height field of the nudging state. The height fields of the ensemble are created by adding random errors with Gaussian distribution mean zero and variance 2π/8 onto the perturbed phase of the initial height of the nudging state. The initial winds of the nudging state and the ensemble members are derived from the initial height fields through the geostrophic relationship.

Figure 2b shows the true initial condition of Case II. The background mean height is 200 m, and the background uniform flow is 10 ms^{-1}. A hyperbolic-shaped height perturbation with a maximum value of 20 m and a length scale of around 100 km, is located in the center of the domain. The wind and height fields are also geostrophically balanced initially. The initial height field of the nudging state moves the true perturbation center westward one grid point and southward two grids points. It adds a random error of Gaussian distribution with mean zero and variance 2.0 onto the true perturbation strength. The initial height fields of the ensemble put random errors with Gaussian distribution mean zero and variance 2.0 onto the perturbation center of the initial nudging state and random errors with Gaussian distribution mean zero and variance 2.0 onto the perturbation strength of the initial nudging state. The initial wind fields are also derived from the initial height fields by means of the geostrophic relationship in both the nudging state and the ensemble.

Periodic boundary conditions are used at the west-east boundaries in both cases. Case I has a free-slip rigid wall boundary condition at the south-north boundaries where height and u-component are defined from the values one point inside the boundary. For Case II, the tendencies of height and wind components are set to zero at the south-north boundaries.

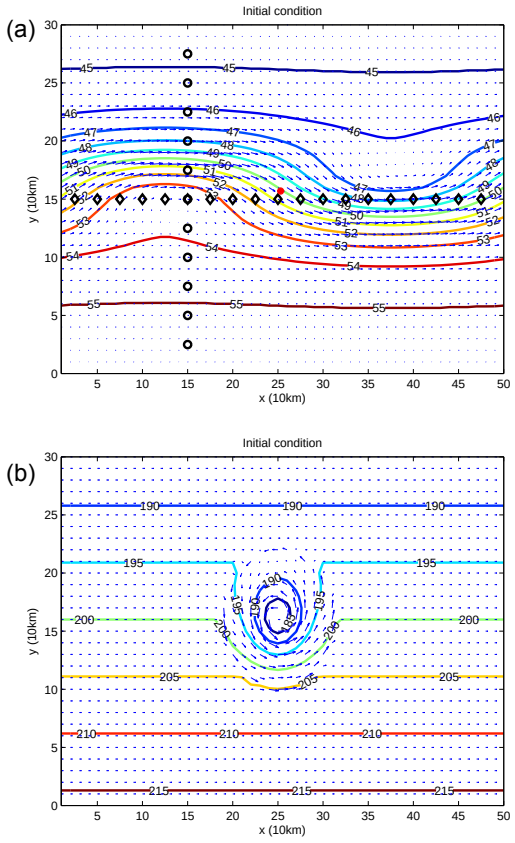

Figure 2. The initial height and wind derived from the initial height using the geostrophic approximation for (a) Case I and (b) Case II. The red dot denotes the observation site of OBSN I, the black diamonds show the observation sites of OBSN II, and the black circles indicate the observation sites of OBSN III.

3.2 *Observations and verification*

Simulated observations representing the "truth" state are generated by finer-scale model simulations. The fine domain has grid spacing of 1 km, grid dimensions of 511×301 and a time step of 1 s. The initial condition and boundary conditions are consistent with the previous discussion in section 3.1. The simulated observations from Case I have variances $\sigma_u^2 = 0.5\ m^2 s^{-2}$, $\sigma_v^2 = 0.5\ m^2 s^{-2}$ and $\sigma_h^2 = 2.5\ m^2$. The variances of the simulated observations in Case II are given as: $\sigma_u^2 = 2.0\ m^2 s^{-2}$, $\sigma_v^2 = 2.0\ m^2 s^{-2}$ and $\sigma_h^2 = 20.0\ m^2$. The simulated observations are produced by adding random errors of Gaussian distribution with mean zero and assumed variances onto the "truth".

Four types of observation networks are tested in this study. The first observation network (OBSN I) has only one randomly chosen observation site, which is shown by the red dot in Fig. 2a, close to the domain center. The second observation network (OBSN II) consists of 19 observations spaced 25 km apart along the center latitude of the domain, and shown by the black diamonds in Fig. 2a. The black circles in Fig. 2a represent the third observation network (OBSN III), which has 11 observations spaced 25 km apart in north-south at x = 150 km. The last observation network (OBSN IV) combines the OBSN II and OBS III together. By default, the observations are available every three hours.

The verification data, based on the 1-km model simulation, is available on every grid point of the 10-km coarse domain. For a given grid point on the coarse domain, the verification data there is the average value of neighboring 10×10 1-km grid points from the fine "truth" domain. The root-mean-square (RMS) errors of height and wind are computed separately every minute. The RMS error decreases slightly with time, because the signal of the unforced wave or vortex is decreased by diffusion gradually in time. Thus a normalized RMS error is used here, which is defined as the RMS error computed against the "truth" run divided by the RMS error of the "truth" computed against its domain-average value. Moreover, a parameter called observation retention (OR) is defined to quantitatively measure the "spikiness" in the error reflecting the ability of the model to retain the observation in the data assimilation. The OR is the average absolute value of the RMS error difference between one time step before the observation time and that at the observation time after the assimilation. In order to take both the RMS error and OR into account, a normalized error parameter, called NER, is calculated by summing the average RMS error normalized by that of the ensemble Kalman smoother (EnKS) and the OR normalized by that of the EnKS. The EnKS is considered the "gold standard" to measure the other assimilation methods. Details will be discussed in section 4.

3.3 *Ensemble covariance inflation and localization*

To avoid filter divergence, an approach is used to increase the background error covariances somewhat by inflating the deviation of the background members with respect to their mean by a small amount as suggested by Hamill et al. (2001). The inflation factor is defined as 1.1. In addition, a covariance localization method is used following Houtekamer and Mitchell (2001), where a fifth-order piecewise rational function is applied to the covariance localization (Gaspari and Cohn 1999). The covariance localization parameter 2c (see Eq. (4.10) of Gaspari and Cohn (1999)) is set to 500 km in Case I, in which 500 km is equal to the wavelength. Similarly, Case II has the covariance

localization parameter 2c set to 100 km, the scale of the initial vortex.

4. RESULTS

Using the two types of initial conditions and cases described in section 3.1, 24-h model integrations are performed with assimilation of 3-hourly observations. The performance of the hybrid EnKF scheme is compared to nudging and EnKF applied separately. The EnKF has the same inflation factor and covariance localization length as the hybrid EnKF as discussed in section 3.3. The nudging radius of influence is given as the covariance localization length of the hybrid EnKF. The nudging coefficients are set to 10^{-4} s^{-1}. Both nudging and hybrid EnKF have a nudging time window of 1 h on each side of the observations. A trapezoidal temporal nudging coefficient function, symmetric around the observation time, with a maximum weight of 1.0 within the center half of the window, decreasing linearly to 0.0 toward the ends of the window, is shown in Fig. 1 and is defined by Stauffer and Seaman (1994).

In addition, an ensemble Kalman smoother (EnKS) is also used in this study (Evensen and Leeuwen 2000). The EnKS is an extended version of EnKF, which uses the solution of the EnKF as the first guess for analysis and applies future observations backward in time to the past model state by using the background ensemble forecasts. Compared to the EnKF, it has the ability of improving model analysis and observation retention, but it requires greater computational cost and data storage. Thus the EnKS is considered our "gold standard" (Lei and Stauffer 2008) to measure the other assimilation methods. As mentioned earlier, this is why the average RMS error and OR of EnKS are used to scale the errors for each method in the computation of the NER. Following Khare et al. (2008), we apply covariance inflation in the EnKS only to the prior estimates of EnKF, and it is also set to 1.1. The ensemble covariance localization of EnKS is the same as EnKF. For efficiency, the EnKS applies each observation backward to the previous observation time every 30 minutes.

Figure 3 shows the normalized RMS error of height and wind in the wave Case I with OBSN II. In both the height and wind fields, the intermittent EnKF scheme shows a significant improvement when observations are assimilated every 3 h, as evidenced by the strong RMS error decreases at the observation times and then followed by a rapid increase in error between the observation times. This pattern is consistent with the 6-h assimilation period results of Fujita et al. (2007). Comparatively, the hybrid EnKF shows RMS error decreasing gradually in time by taking advantage of the continuous nudging approach. The RMS errors of the hybrid EnKF are lower than those of EnKF after the first time the observations are assimilated. The pink dash-dot spikes of EnKS every 30 minutes apart denote the improvement in RMS error obtained from the next available observation which is applied back to previous observation time. Since the next observation is applied backward only to the previous observation time every 30 minutes in EnKS, the normalized RMS error of EnKS has similar performance to that of EnKF, where large error corrections are made when observations are assimilated. Thus here the hybrid EnKF produces smaller RMS error than both EnKF and EnKS, and it also produces smoother analyses in time than both EnKF and EnKS.

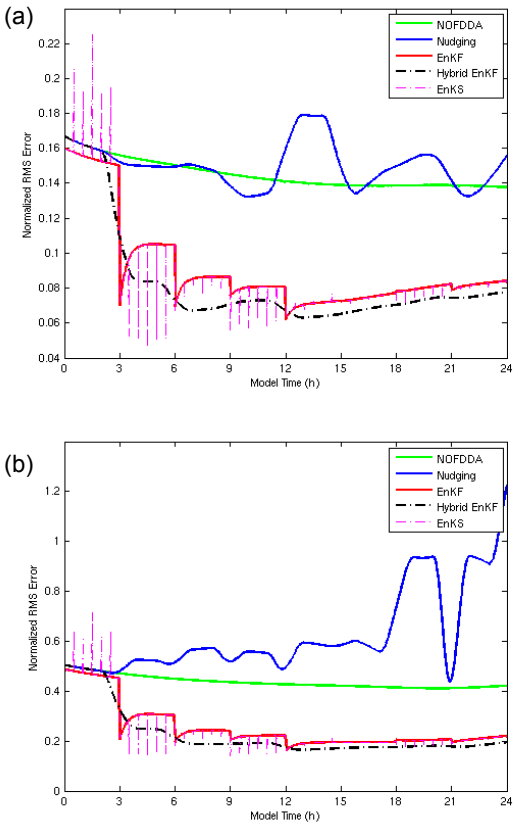

Figure 3. The normalized RMS error of Case I using OBSN II for (a) height field and (b) wind field. The green solid line is the normalized RMS error using no data assimilation, the blue solid line is that of nudging, the red solid line is that of EnKF, the black dash-dotted line is that of hybrid EnKF, and the pink dash-dotted line is that of EnKS.

The average values of RMS error, OR and NER over the 24-h period for Case I using different observation networks for data assimilation are shown in Fig. 4. Figures 4a and 4d show that the hybrid EnKF produces the smallest average RMS error in both the height and wind fields. Figures 4b and 4e indicate that the hybrid EnKF has the smallest values of OR, i.e. the best observation retention. The EnKF and EnKS have much larger values of OR than both nudging and hybrid EnKF. The EnKS usually has smaller RMS errors than the EnKF at analysis steps due to future observations being applied backward. Thus the hybrid EnKF retains the benefit of EnKF to reduce the RMS error effectively, obtains better observation retention and produces a smoother solution in time with smaller discontinuities

than EnKF by use of nudging-type terms to apply the EnKF continuously in time. Moreover, the hybrid EnKF also has the smallest values of NER, since it has the smallest average RMS error and the smallest value of OR.

The normalized RMS errors of height and wind for the moving vortex Case II with OBSN II are shown in Fig. 5. It is interesting that using no data assimilation (NOFDDA) performs best for the height field after the first two observation times. Following the third observation time (9 h), the hybrid EnKF shows a clear RMS error improvement over all the other data assimilation schemes. The wind field, on the other hand, responds more favorably to data assimilation methods early in the simulations, and strong corrections by the EnKF at observation times are once again seen in the wind field. Similar to the wave case shown in Fig. 3b, the hybrid EnKF reduces the RMS wind error in the vortex case gradually in time with fewer and weaker discontinuities compared to the EnKF.

Figure 6 exhibits the average values of RMS error, OR and NER for Case II assimilating the different observation networks. The hybrid EnKF also produces the smallest average RMS error in OBSN II and OBSN IV. However in OBSN I and OBSN III, the hybrid EnKF produces somewhat larger average RMS error than the EnKF and EnKS. This is because the error reduction in the EnKF and EnKS mainly comes from ensemble averaging. The observations in OBSN I and OBSN III play a much reduced role compared to the larger number of observations along the flow in OBSN II and OBSN IV. The OBSN I and OBSN III networks cannot detect the moving vortex sufficiently. Nonetheless, as shown by Figs. 6b and 6e, the hybrid EnKF has the best (lowest) OR even with OBSN I and OBSN III. In addition, the hybrid EnKF produces better (smaller) values of NER than both EnKF and EnKS, as shown in Figs. 6c and 6f.

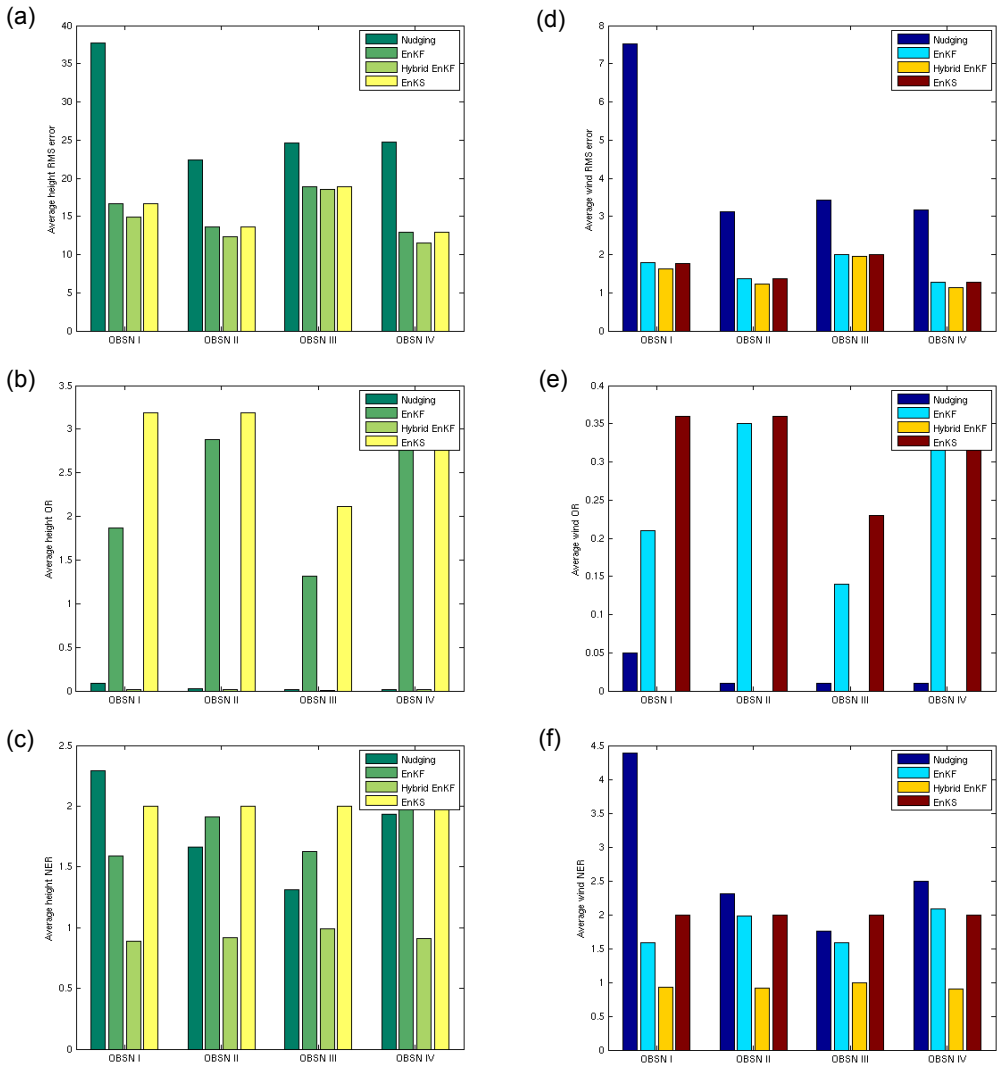

Figure 4. Height and wind statistics for Case I with different observation networks: (a) the average height RMS error, (b) the average height OR, and (c) the height NER, (d) the average wind RMS error, (e) the average wind OR, and (f) the wind NER. Smaller values are better values for all three statistics.

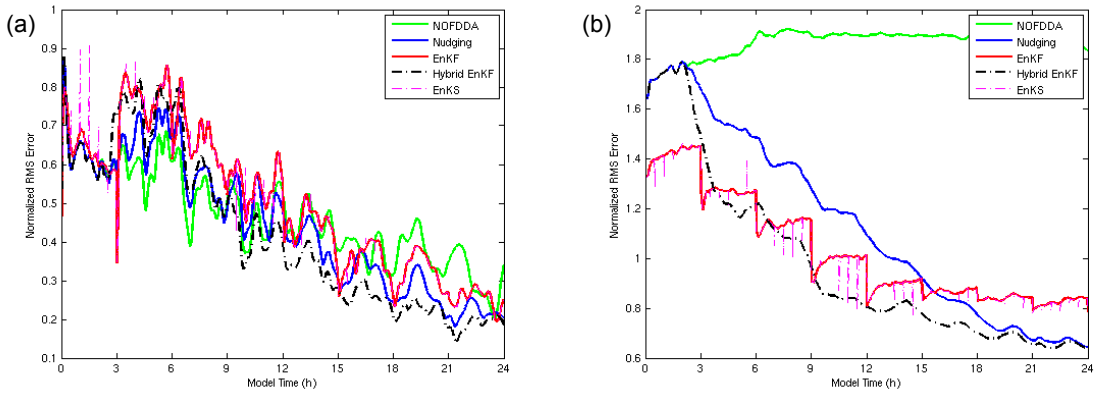

Figure 5. Same as Fig. 3, except for Case II using OBSN II.

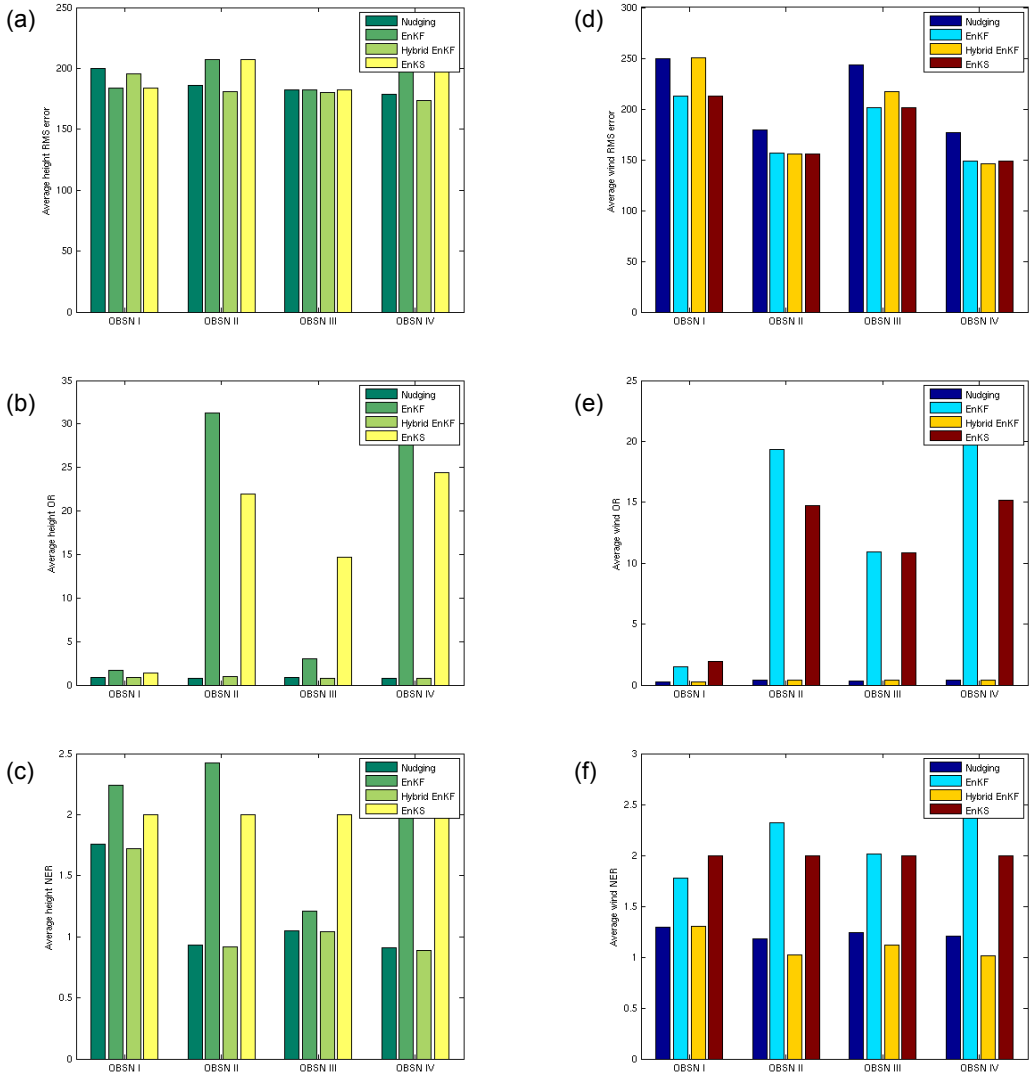

Figure 6. Same as Fig. 4, except for Case II.

5. CONCLUSIONS AND DISCUSSION

A hybrid EnKF data assimilation approach is investigated using a 2D shallow water model and building on that learned from a Lorenz three-variable model system (Lei and Stauffer 2007; 2008). A quasi-stationary wave case and a moving vortex case are used to further test the hybrid EnKF scheme. Four observation networks are applied in the 24-h data assimilation experiments for each case. The hybrid EnKF reduces the RMS error more significantly than the EnKF. Moreover, the hybrid EnKF retains the benefits from the continuous nudging approach to improve the model state gradually rather than make strong corrections and discontinuities at the analysis steps as the EnKF. Compared to the "gold standard" EnKS, the hybrid EnKF has the ability to reduce the RMS error as good as or even better than the EnKS, and also produce better observation retention than the EnKS at a reduced computational cost which is more similar to that of the EnKF.

6. ACKNOWLEDGEMENTS

This research is supported by DTRA contract no. HDTRA1-07-C-0076 and Dr. John Hannan of DTRA. The authors would like to thank Aijun Deng, Sue Ellen Haupt, George S. Young and Fuqing Zhang for helpful discussions and comments.

7. REFERENCES

Anderson, J. L., 2001: An ensemble adjustment Kalman filter for data assimilation. *Mon. Wea. Rev.*, **129**, 2884-2903.

Duane, G. S., J. J. Tribbia, and J. B. Weiss, 2006: Synchronicity in predictive modeling: a new view of data assimilation. *Nonlin. Processes Geophys.*, **13**, 601-612.

Evensen, G., 1994: Sequential data assimilation with a nonlinear quasigeostrophic model using Monte Carlo methods to forecast error statistics. *J. Geophys. Res.*, **99** (C5), 10143-10162.

Evensen, G., and P. J. van Leeuwen, 2000: An ensemble Kalman smoother for nonlinear dynamics. *Mon. Wea. Rev.*, **128**, 1852-1867.

Fujita, T., D. J. Stensrud, and D. C. Dowell, 2007: Surface data assimilation using an ensemble Kalman filter approach with initial condition and model physics uncertainties. *Mon. Wea. Rev.*, **135**, 1846-1868.

Gaspari, G., and S. E. Cohn, 1999: Construction of correlation functions in two and three dimensions. *Quart. J. Roy. Meteor. Soc.*, **125**, 723-757.

Grammeltvedt, A., 1969: A survey of finite-difference schemes for the primitive equations for a barotropic fluid. *Mon. Wea. Rev.*, **97**, 384-404.

Hamill, T. M., J. S. Whitaker, and C. Snyder, 2001: Distance-dependent filtering of background error covariance estimates in an ensemble Kalman filter. *Mon. Wea. Rev.*, **129**, 796-811.

Houtekamer, P. L., and H. L. Mitchell, 1998: Data assimilation using an ensemble Kalman filter technique. *Mon. Wea. Rev.*, **126**, 796-811.

Houtekamer, P. L., and H. L. Mitchell, 2001: A sequential ensemble Kalman filter for atmospheric data assimilation. *Mon. Wea. Rev.*, **129**, 123-137.

Hunt, B. R., E. Kalnay, E. J. Kostelich, E. Ott, D. J. Patil, T. Sauer, I. Szunyogh, J. A. Yorke and A. V. Zimin, 2004: Four-dimensional ensemble Kalman filtering. *Tellus*, **56A**, 273-277.

Juckes, M., and B. Lawrence, 2009: Inferred variables in data assimilation: quantifying sensitivity to inaccurate error statistics. *Tellus*, **61A**, 129-143.

Khare, S. P., J. L. Anderson, T. J. Hoar, and D. Nychka, 2008: An investigation into the application of an ensemble Kalman smoother to high-dimensional geophysical systems. *Tellus*, **60A**, 97-112.

Lei, L., and D. Stauffer, 2007: A hybrid nudging-EnKF approach to data assimilation. *22nd Conference on Weather Analysis and Forecasting / 18th Conference on Numerical Weather Prediction*, Park City, Utah, Amer. Metero. Soc., 8 pp.

Lei, L., and D. Stauffer, 2008: An incremental ensemble Kalman filter approach to data assimilation. *2008 Chemical and Biological Defense Physical Sscience and Technology Conference*, New Orleans, Louisiana, 3 pp.

Stauffer, D. R., and N. L. Seaman, 1990: Use of four-dimensional data assimilation in a limited-area mesoscale model. Part I: Experiments with synoptic data. *Mon. Wea. Rev.,* **118**, 1250-1277.

Stauffer, D. R., and N. L. Seaman, 1994: Multiscale four-dimensional data assimilation. *J. Appl. Meteor.,* **33**, 416-434.

Whitaker, J. S., and T. M. Hamill, 2002: Ensemble data assimilation without perturbed observations. *Mon. Wea. Rev.*, **130**, 5132-5147.

Zhu, K., I. M. Navon and X. Zou, 1994: Variational data assimilation with a variable resolution finite-element shallow-water equations mode. *Mon. Wea. Rev.*, **122**, 946-965.